



LAWRENCE
LIVERMORE
NATIONAL
LABORATORY

Determination of diffusion profiles in altered wellbore cement using XRCT methods

H. E. Mason, W. L. DuFrane, S. D. C. Walsh, S. A. Carroll

December 16, 2013

Environmental Science and Technology

Disclaimer

This document was prepared as an account of work sponsored by an agency of the United States government. Neither the United States government nor Lawrence Livermore National Security, LLC, nor any of their employees makes any warranty, expressed or implied, or assumes any legal liability or responsibility for the accuracy, completeness, or usefulness of any information, apparatus, product, or process disclosed, or represents that its use would not infringe privately owned rights. Reference herein to any specific commercial product, process, or service by trade name, trademark, manufacturer, or otherwise does not necessarily constitute or imply its endorsement, recommendation, or favoring by the United States government or Lawrence Livermore National Security, LLC. The views and opinions of authors expressed herein do not necessarily state or reflect those of the United States government or Lawrence Livermore National Security, LLC, and shall not be used for advertising or product endorsement purposes.

Determination of diffusion profiles in altered wellbore cement using XRCT methods

Harris E. Mason^{1,*}, Stuart D. C. Walsh¹, Wyatt L. DuFrane¹, and Susan A. Carroll¹

¹Physical and Life Sciences Directorate, Lawrence Livermore National Laboratory

*corresponding author: mason42@llnl.gov

ABSTRACT

The development of accurate, predictive models for use in determining wellbore integrity require detailed information about the chemical and mechanical changes occurring in hardened Portland cements. X-ray computed tomography (XRCT) provides a method that can non-destructively probe these changes in three dimensions. Here we describe a method for extracting sub-voxel mineralogical and chemical information from synchrotron XRCT images by combining advanced image segmentation with geochemical models of cement alteration. The method relies on determining 'effective linear activity coefficients' (ELAC) for the white light source to generate calibration curves that relate the image grayscales to material composition. The resulting data set supports the modeling of cement alteration by CO₂-rich brine with discrete increases in calcium concentration at reaction boundaries. The results of these XRCT analyses can be used to further improve coupled geochemical and mechanical models of cement alteration in the wellbore environment.

INTRODUCTION

Portland cements are commonly employed in primary cementing operations in wellbores to isolate deep storage or hydrocarbon production fluids from underground source of drinking water. The focus of our work is to better understand how chemical and mechanical alteration of

wellbore cements in geologic carbon storage environments impact leakage of storage fluids and gases. Reaction of Portland cement with CO₂-rich brines yields three distinct alteration zones consisting of portlandite-depleted (CH-depleted), carbonate, and residual amorphous silicate regions, where the portlandite-depleted and amorphous silicate regions have lower bulk moduli and hardness than the unreacted cement and the carbonate layers.¹⁻⁴ Currently, there is no consensus on why experiments generally show a decrease in permeability when reacted with CO₂-rich brines. We argue that the observed decrease in wellbore permeability reflects weakening and compression of the chemically altered fracture asperities causing the hydraulic aperture to decrease.⁴ Elsewhere, replacement of portlandite with higher molar volume calcite⁵⁻⁸ or expansion of the amorphous silicate zone⁹ have also been attributed to the decrease in well permeability in CO₂-storage environments. Understanding the effects of carbonated brine on wellbore cement is also of concern to the geothermal industry (both for wells in naturally CO₂-rich geothermal fields¹⁰⁻¹³ and novel geothermal plants that propose CO₂ as an alternative heat exchange fluid^{14, 15}), and to the oil industry where CO₂ is used for enhanced oil recovery.¹⁶

X-ray computed tomography (XRCT) lends itself to the study of mineral alteration and cement alteration in particular, because the spatial distribution of the alteration layers with varying densities and compositions can be resolved nondestructively.^{3, 9, 17-19} The grayscale of XRCT voxels are related to the elemental composition and density of the material contained within the representative volume. Partial volume effects where the voxel grayscale is representative of a combination of materials can also be exploited to deconvolve multiple constituents at sub-voxel resolutions.²⁰⁻²⁵ XRCT can also be used to assess mechanical deformation that occurred during experiment when combined with digital imaging correlation using a particle image velocimetry technique.^{4, 26} Walsh et al.³ used time dependent solution

chemistry and the spatial distribution of the altered layers to develop chemical model for the alteration of wellbore cement. This model assumed uniform mineral composition, porosity, tortuosity, and effective diffusivity for each layer based on near uniform grayscale in the tomography data.

In this study, we test the assumptions used in these chemical and mechanical models using sophisticated image segmentation methods of XRCT data sets combined with geochemical models of cement alteration. The result is detailed, sub-voxel spatial information about the distribution of the materials present in altered cement. This data is further used to derive elemental profiles through the reaction layers. The observations in this study show that the uniform models, such as those proposed by Walsh et al.³ that describe layer boundaries in terms of an increase in Ca concentration, appropriately describe the reactions observed in these cement samples.³ We also discuss the potential for these data to further constrain both chemical and geomechanical models of wellbore integrity.

METHODS

The samples consisted of two mated half cores of cement and of fully dense sandstone caprock that were separated by artificially created fracture apertures. The flow-through experimental setup and the detailed geochemical results are described in detail in Walsh et al.³ The cement half core of samples were abraded with glass beads to produce a roughened fracture surface of variable aperture. A solution of CO₂ saturated brine was flowed along the fracture aperture in the cement/caprock for a period of 8 days. At the end of this time, the samples were removed and allowed to dry under ambient conditions. These samples were imaged before and after reaction with the CO₂ saturated brine at the 8.3.2 beamline at the Advanced Lightsource (ALS; Berkeley, California) using a whitelight synchrotron X-ray source. The initial beam was

prefiltered using a 3 mm thick Al filter closer to the injection of the beam, and a 2 mm Al and 0.5 mm Cu filter close to the sample. These experiments produced an initial image stack with a 4.5 μm voxel size that was then downsampled to a more computationally manageable sized stack with a final voxel size of $\sim 18 \mu\text{m}$. An example image slice is presented in Figure S1. Due to the heterogeneities within the reaction layers, simple grayscale thresholding is insufficient to segment the reaction layers; therefore, reaction layer segmentation was first performed using the Fiji processing software with the user guided Weka Segmentation procedure.²⁷ Empirical corrections for beam hardening were obtained by fitting average radial grayscale values for the more uniform sandstone half of the core (Figure S2) and subtracting synthetic images generated with the fitted radial distribution from the experimental images.

In order to adjust for the use of a white light source, we calculate effective linear activity coefficients for the various cement materials we will be employing in our model. We can calculate the flux of the X-rays from the source at the chosen energies²⁸ (Figure 1a), and knowing the composition and thicknesses of the metal filters, and the linear activity coefficients for these metals at these energies, we can calculate the flux that reaches the sample with the Beer-Lambert Law.

$$I = I_0 e^{-(\mu/\rho)l} \quad (1)$$

I is the final flux, I_0 is the initial flux, μ/ρ is the linear activity coefficient, and l is the path length through the material (in this case the thickness of the filters). The result is an asymmetric curve with its peak at 30 keV (Figure 1b). Theoretical linear activity coefficients were calculated at each of the 8 X-ray energies for the materials listed in Table 1 by linearly adding the weighted LAC for each element in the material based on their atomic compositions, and dividing these by

the material density.²⁹ These values were further weighted by the relative X-ray flux at each of these energies. We refer to these values as the “effective” linear activity coefficients (ELAC; Table 1) and use these values to estimate material proportions from our XRCT images.

The ELAC values obtained for the materials listed in Table 1 were derived from a calibration curve based on the composition and grayscale values of particular grains in these XRCT images (Figure S3). For instance, the brightest spots within the cement and caprock regions can be easily assigned to C₃S and pyrite mineral grains, respectively. The darkest spots are air contained in void spaces. We can also average over a region of the unreacted cement to get an average grayscale for this material. If we plot the grayscale values obtained for these materials as a function of their density we see that we do not get a suitable linear calibration curve (Figure 2a). This plot shows that many materials have a similar density in the cement, but have differing compositions that give rise to the differences in grayscales observed. Instead if we plot these grayscales as a function of ELAC we obtain a suitable calibration curve (Figure 2b). We can use the relationship from this curve to define linear mixing relationships between two materials, as well as determine the grayscales for the additional cement materials in Table 1.

Elemental analyses of a similarly reacted cement sample were obtained on a gold coated thin section of the cement half core and analyzed with scanning electron microscopy (SEM) and X-ray energy dispersive spectroscopy (EDS). These analyses were performed at 20 kV under a FEI Inspect F scanning electron microscope equipped with an Everhart-Thornley secondary-electron detector, a solid state diode backscattered-electron detector and an EDAX APOLLO XL X-ray detector with energy resolution better than 133 eV at Mn-K and an active area of 30 mm². Additional experimental details about this sample are presented in Mason et al.²

RESULTS AND DISCUSSION

The application of the ELAC to the reacted cement images requires at least a basic knowledge of what materials are present in each reaction layer, and if possible some knowledge of the volume percentages of each mineral. In our previous papers, we developed detailed geochemical models of cement alteration in the presence of CO₂-rich brines as well as determined the mineralogical composition of the unreacted cement² (Table 2). These models can be used in advanced segmentation methods to further constrain the material composition of each of the reaction layers. The approach we have developed is to first implement a larger scaled segmentation of the reacted cement images to obtain the extents of the reaction layers (Figure 3a,b). These extents are then used as image masks where we the previously defined chemical models are used to define the material composition of these layers. In the subsequent sections, we will discuss the composition of each layer and how we can use the ELAC values we have determined combined with the geochemical models of cement alteration.

Segmenting the amorphous, carbonate, and depleted layers

In our previous work, we found that the conversion of the CSH to an amorphous zeolite is complete within the carbonate layer, and that as a first order approximation we can adequately describe the amorphous layer and carbonate layers as containing only polymorphs of CaCO₃, an amorphous aluminosilicate, and developed pore space.^{2, 3} The other cement minerals are either assumed to have dissolved to form these materials or be in low, inconsequential abundance. Our recent findings indicate that the Si and Al solution chemistry data is best fit with the Ca-free mineral analcime.³ However, we model the amorphous material as the mineral mordenite based on our previous observations that there is some residual Ca within the amorphous layer with

EDS.² Both minerals have a similar ELAC (Table 1) and it would be impossible to differentiate between them with the current methods. In reality, the material is thermodynamically similar to analcime, but contains residual Ca in its structure. With these assignments we assume the grayscales are due to linear mixtures of these materials at subvoxel resolution due to partial volume effects and that we can describe the grayscales for individual voxels using simple mixing relationships. We assume that regions brighter than that assigned to the amorphous material are fully dense with CaCO₃ completely filling the intergranular spaces left behind by the dissolution of portlandite. Therefore, we describe the voxel attenuation (μ_{vox}) between these values by a simple linear combination of amorphous material (μ_{am}) and CaCO₃ (μ_{cc}).

$$\mu_{vox} = f \cdot \mu_{am} + (1 - f) \cdot \mu_{cc} \quad (2)$$

Conversely, we assign grayscale values with values equal to or lesser than that of the amorphous material as a linear mixing of the amorphous material and pore space that developed from CaCO₃ dissolution.

$$\mu_{vox} = f \cdot \mu_{pore} + (1 - f) \cdot \mu_{am} \quad (3)$$

Similar methods have been used previously to distinguish mineral and microporosity contributions to image grayscale.^{20, 21}

The ELAC values we have determined are based on both the chemical composition and density of the material. In the instance of materials such as CaCO₃ it becomes clear that the structural polymorph used in these segmentations is important. In our previous work, we X-ray powder diffraction indicated the presence of aragonite in combination with calcite in the carbonate layer of a reacted wellbore cement.² Aragonite has a higher density of 2.95 cm³/g than calcite with a density of 2.71 cm³/g. Therefore, despite having the same composition, areas that

contain aragonite will appear brighter in the XRCT images than areas containing calcite. In these images, the ELAC value for aragonite is required to adequately account for the grayscales we observe in the carbonate layer (Figure S4). It is unlikely that the carbonate layer contains only aragonite, and these voxels are a mixture of calcite and aragonite. However, given the additional complication of the amorphous material it is difficult to assign discrete phase abundances to the two carbonate materials. We must then for simplicity use the aragonite phase for these determinations despite a mixture being present.

Using these models we are able to produce specific mineral maps for the combined amorphous and carbonate layers that illustrate the distribution of these minerals through these two layers (Figure 3c,d). We observe that CaCO_3 is distributed only within the masked area designated for the carbonate layer, and that it is most concentrated at the boundary with the portlandite depleted zone. The 3D analyses indicate that the amorphous material is concentrated at the boundary with the carbonate zone and along desiccation cracks (Figure 4). We attribute the higher concentration of this material at the carbonate layer boundary to the presence of CaCO_3 buffering the pH and making the amorphous phase less soluble in this layer. In the absence of this buffer, the amorphous material is susceptible to dissolution allowing pore space to develop between grains. Higher concentrations at the desiccation cracks are attributed to the collapse of pore space upon drying.

Similarly, we can analyze the portlandite depleted layer and the unreacted cement layer together in the same segmentation. Our geochemical model indicates that the only mineralogical difference between the unreacted cement and the portlandite depleted zone is the loss of portlandite. All other mineralogical assemblages are assumed to remain unchanged. We define

grayscale zones where linear mixing terms can be defined, similar to our treatment of the amorphous/carbonate layers.

For these segmentations we use threshold levels defined by grayscales in ascending order for pore space, CSH, portlandite depleted cement, unreacted cement, and C₃S. The grayscale for the portlandite depleted cement is set as:

$$\mu_{depl} = \mu_{cem} - 0.196 \cdot \mu_{CH} + 0.196 \cdot \mu_{pore} \quad (4)$$

This model is based on our prior characterization of the unreacted cement that indicates a bulk portlandite content of 19.6 volume %, and assumes that the amount removed to generate pore space cannot exceed this value. Despite the higher ELAC value for portlandite (Table 1), we do not set up mixing between the cement and portlandite since the portlandite grains in fully cured Portland cement are generally smaller than the voxel size of our XRCT measurements³⁰⁻³² and will contribute to the unreacted cement grayscale. The same justification is applied to the other minor constituents such as ettringite, and aluminate phases. Combining the segmentation of the amorphous and carbonate zones with these two additional layers gives a complete picture of how the cement constituents are distributed throughout the cement half and generates a map of the developed pore space resulting from cement alteration (Figure 3e). With the images segmented into the cement constituents at a subvoxel resolution, we gain more detailed spatial information about the chemical reactions that occur between the brine and the cement half core.

Mapping Ca-concentrations.

The reactions occurring between the CO₂-rich brine are dominated by the precipitation and dissolution of Ca-rich minerals. One important use for the segmented images derived above is to produce maps of the relative Ca concentration changes through the cement to track the

spatial alteration of the cement. Conversion of mineral distributions to Ca-concentrations is made by dividing the volume percentage of the minerals by their respective molar volumes (Table 1). By linearly adding the volume weighted Ca contributions from each mineral we can obtain the Ca-concentration in each voxel and generate a map that shows the relative Ca concentrations through the cement half of the core (Figure 5a). This image shows sharp changes in Ca-concentration between the layer boundaries where clear jumps have occurred in the relative abundances of Ca-containing minerals. Concentration profiles across the reaction zones can also be generated from these maps (Figure 5b). These profiles show that as the reaction front moves from the fracture surface, a highly Ca-depleted amorphous zone occurs, followed by a peak in the Ca concentration corresponding to the development of a Ca-rich carbonate layer. Next, a distinctive trough is observed in the portlandite depleted zone and a gradual rise to the unreacted cement layers. The boundaries between layers in the Ca-profile appear more gradual than what is presented in the Ca-concentration map, due to averaging over boundaries that are slightly arched. These data mirror EDS data collected for a similarly reacted cement/caprock core and indicate the methods developed here adequately capture the Ca concentration changes occurring due to these reactions (Figure 5d and e).

Implications on wellbore integrity modeling

Portland cement presents unique challenges for geochemical studies due to their complex, heterogeneous composition, the strong dependency of composition on curing conditions, and their strong reactivity in the wellbore environment at CO₂ storage sites. XRCT has provided a non-destructive technique that has allowed numerous groups to investigate the chemical and structural impact that CO₂-rich brine leakage can have on these materials.^{2-4, 18, 19, 26} The advanced segmentation methods based on the ELAC values and geochemical models outlined

here have the potential to refine the geochemical models presented in these studies by providing sub-voxel compositional information allowing the 3D distribution of alteration products to be determined non-destructively.

In our previous work, we developed reactive transport and geomechanical models for wellbore cement alteration based partly on the results from XRCT imaging.^{3, 4, 26} The uniformity of the XRCT grayscales over the reaction zones support a simplified chemical model where reactions occur only along the zone boundaries and each layer was made up of a uniform mineral composition, porosity, tortuosity, and effective diffusivity. Application of ELAC values to the grayscale data indicate sharp transitions in the Ca concentrations at the reaction boundaries followed by uniform average concentrations over the reaction zone. This result supports an equilibrium-controlled moving front model, because kinetically controlled reactions would likely produce gradations in Ca concentrations along the diffusion front. The ELAC analysis allows such information to be gathered in 3D without destroying the sample. Further, the sub-voxel mineral and pore distribution maps provide much needed constraints for geomechanical models. Currently, the geomechanical models developed rely on empirically derived values for bulk moduli.⁴ Better estimates of the mechanical properties of each layer could be derived combining specific mineral and pore properties based on 3D distributions derived from the ELAC analysis of the tomography data. Such parameter constraint is needed for accurate assessment of long term wellbore stability because the mechanical property of the cement changes as a consequence of reaction with the CO₂-rich brine.

ACKNOWLEDGEMENTS

We gratefully support for this work under the DOE National Energy Technology Laboratory,
Project AA3030100. The Advanced Light Source is supported by the Director, Office of Basic
Energy Sciences of the US Department of Energy under Contract N. DE-AC0-2-05CH11231.
We thank A. MacDowell and D. Parkinson for their assistance at the beamline. We would like to
thank M. Smith for assistance with the initial setup of the core-flood experiment, Z. Dai for
assistance with performing SEM/EDS analyses, S. Torres and D. Ruddle for preparation of
sample cores, and L. Knauer and the California Well Sample Repository for the caprock
samples. This work was performed by LLNL under Contract DE-AC52-07NA27344.

256 **Table 1.** Materials used in this study and their corresponding densities, effective linear activity
 257 coefficients, and molar volumes.

Material	Composition	Density (g/cm ³)	ELAC	MV (cm ³ /mol Ca)
Pores (air)	-	0	0	-
Analcime	Na _{0.96} Al _{0.96} Si _{2.04} O ₆ • H ₂ O	2.24	1.63	-
Mordenite	Ca _{0.28} Na _{0.36} Al _{0.94} Si _{5.06} O ₁₂ • 3.47 H ₂ O	2.15	1.72	405
Ettringite	Ca ₆ Al ₂ (SO ₄) ₃ (OH) ₁₂ • 12 H ₂ O	1.70	1.91	246
CSH	Ca _{1.7} SiO _{3.7} • 1.5 H ₂ O	2.12	3.01	63.1
Cement	See Table 2	2.05	3.78	38.5
Calcite	CaCO ₃	2.71	4.35	36.9
Portlandite	Ca(OH) ₂	2.24	4.57	33.1
Aragonite	CaCO ₃	2.95	4.73	33.9
C₄AF	Ca ₄ (Al,Fe) ₄ O ₁₀	3.03	5.66	32.6
C₃S	Ca ₃ SiO ₅	3.21	6.74	23.7
Pyrite	FeS ₂	4.80	19.7	-

258
 259 **Table 2.** Average composition of the unreacted cement. Adapted from Walsh et al 2013.

Mineral	Weight %	Volume %
CSH	57.1	53.3
Portlandite	19.6	17.2
Calcite	13.5	9.8
C₃S	6.5	4.0
C₄AF	2.3	1.2
Ettringite	0.9	1.0
Porosity	-	14.0

260

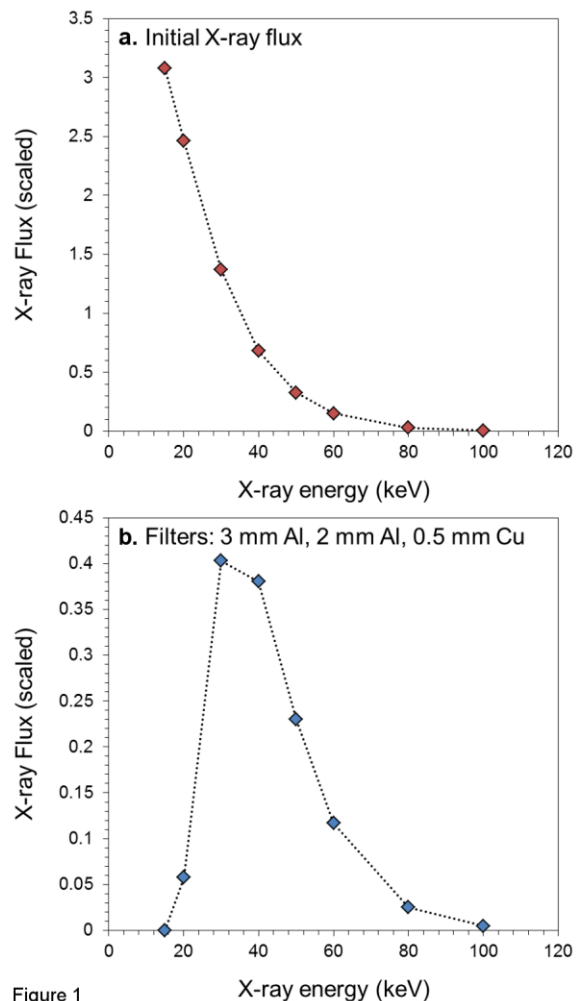


Figure 1

Figure 1. Scaled X-ray fluxes chosen at eight discrete X-ray energies from the ALS Beamline 8.3.2 **a.** Calculated incoming fluxes from 1.3 GeV, 500 mA ring current after passing through the 4.37 T bending magnet into the beamline. **b.** Attenuated energies after passing through the listed filters that reach the core sample. The dotted lines are provided to guide the eyes.

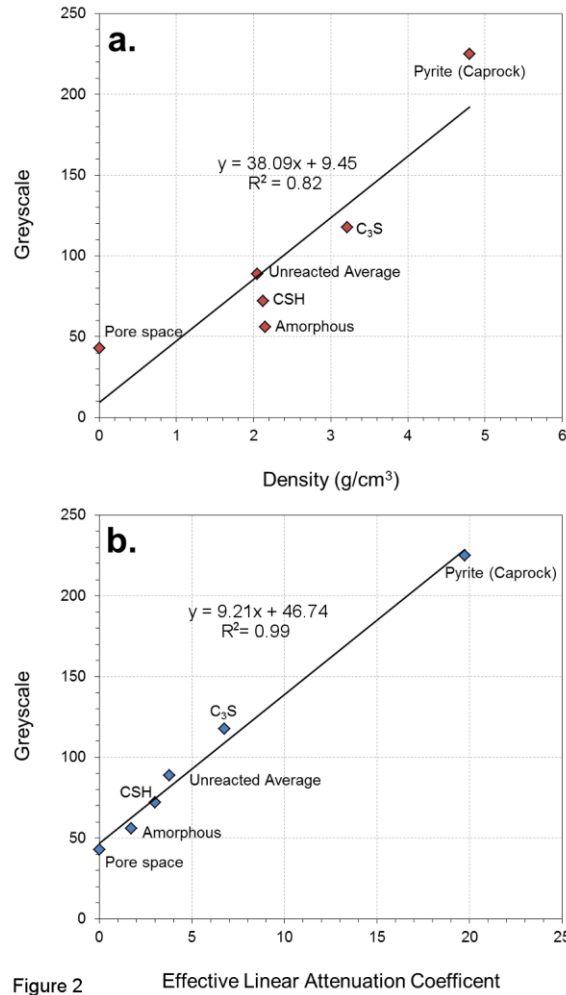


Figure 2

Figure 2. Tomography grayscale calibration curves that were generated **a.** using materials densities (g/cm^3), and **b.** using the effective linear activity coefficients of the labeled materials. Solid lines represent linear fits to the data points. The corresponding equations and R^2 values of these fits are also given.

272

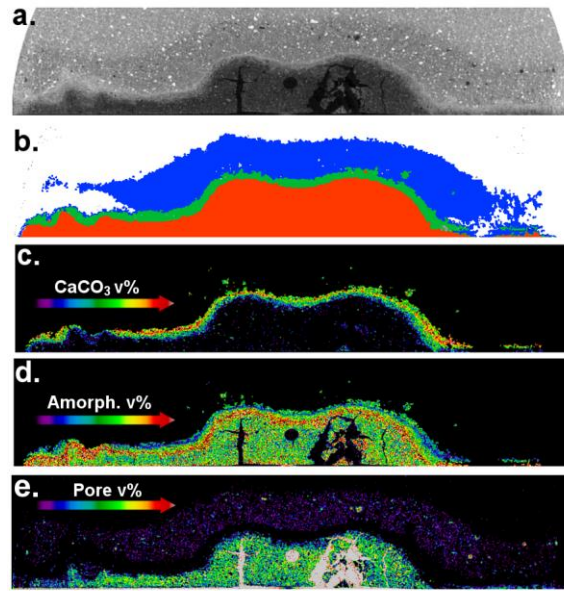


Figure 3

273

274

Figure 3. Results of the segmentation for a slice from the XRCT image stack for the carbonate and amorphous layers. **a.** Cropped section from of the original image isolating the reaction layers. **b.** Corresponding colorized mask showing the extents of the amorphous (red), carbonate (green), and CH depleted (blue) layers. **c.** Colorized map of corresponding to the volume percentage (v%) of CaCO_3 . **d.** Colorized map corresponding to volume percentage of the amorphous material. **e.** Colorized map corresponding to volume percentage corresponding to sub-voxel porosity developed in the reaction layers. Increased volume percentage of material is indicated by the corresponding color bar (grading from black at 0 v% to gray at 100 v%).

282

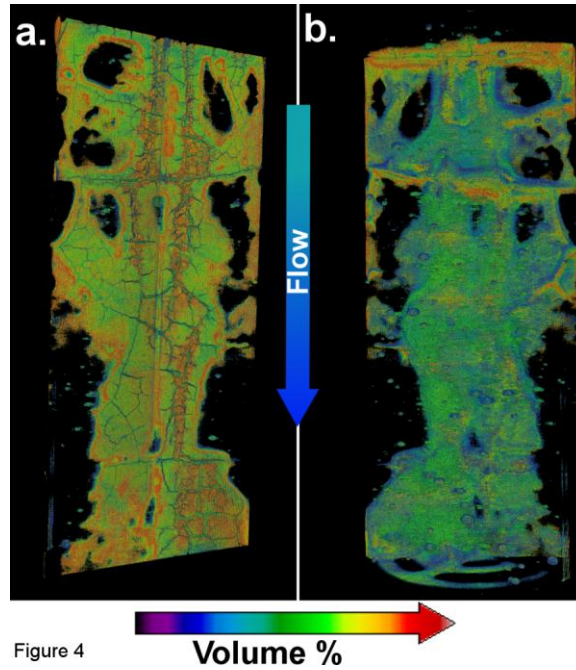


Figure 4

Figure 4. 3D representation of the amorphous material distributed along the length of the core.

a. View at the boundary with the fracture surface. **b.** View at the boundary of the carbonate layer. Blue arrow indicates the direction of fluid flow during the experiment, and rainbow arrow indicates increase in volume percent of the amorphous material (grading from black at 0 v% to red at 100 v%).

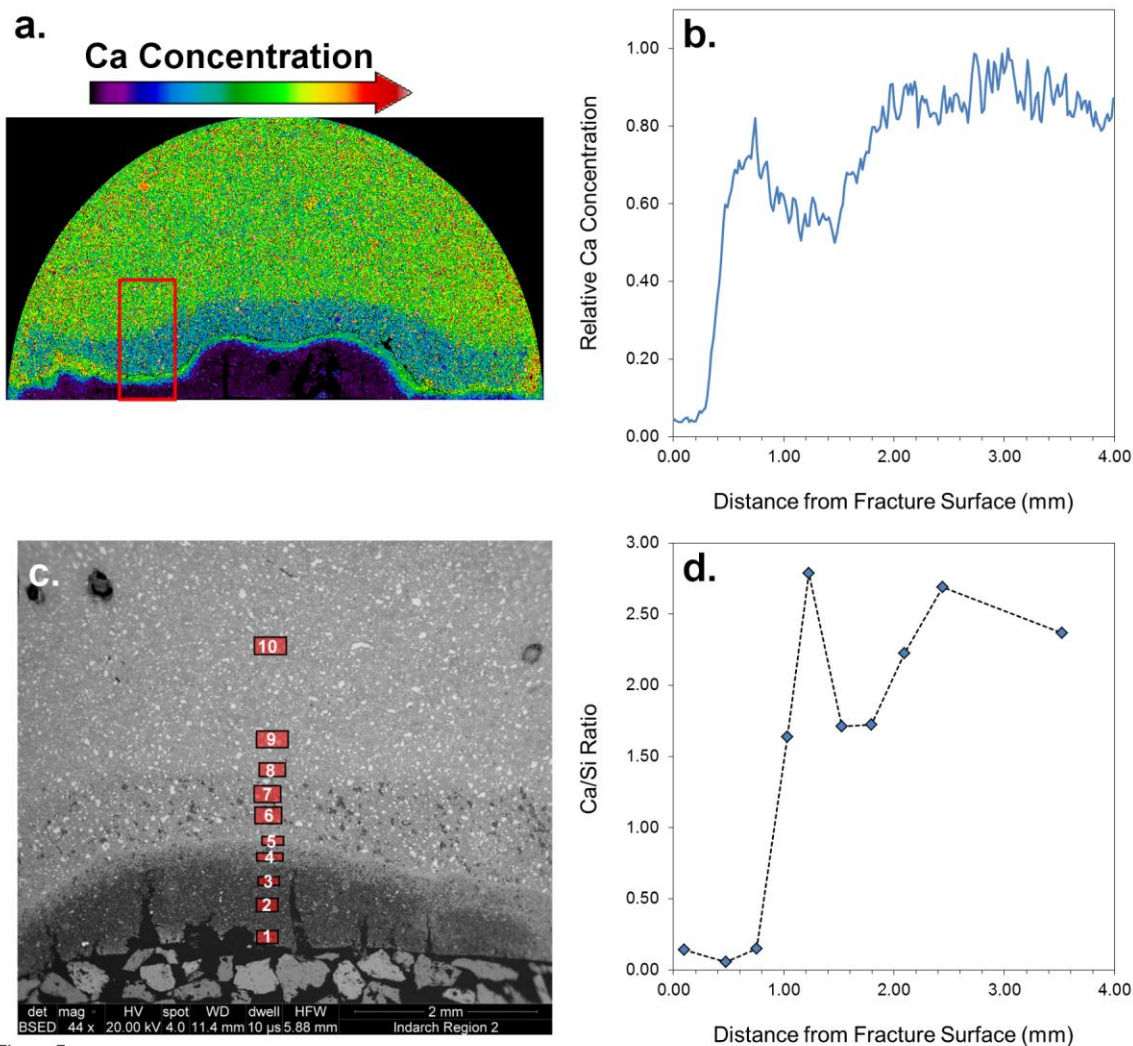


Figure 5

Figure 5. Comparison of the Ca concentrations obtained with tomographic image processing with EDS derived values. **a.** Colorized image slice with increasing relative Ca concentration indicated by the corresponding color bar (grading from black at 0 v% to red at 100 v%). The red box indicates the region summed over to produce the concentration profile. **b.** Relative Ca concentration profile for summed over a region of the segmented image. The values are normalized to the highest summed intensity **c.** SEM image of the polished thin slice with the locations of the EDS rasters labeled in ascending order from the fracture surface. **d.** Ca/Si ratios

299 derived from EDS rasters obtained on the corresponding polished thin section of an altered
300 cement sample.

301

302 REFERENCES

- 303 1. Kutchko, B. G.; Strazisar, B. R.; Dzombak, D. A.; Lowry, G. V.; Thaulow, N., Degradation of
 304 well cement by CO₂ under geologic sequestration conditions. *Environmental Science & Technology* **2007**,
 305 *41*, (13), 4787-4792.
- 306 2. Mason, H. E.; Du Frane, W. L.; Walsh, S. D. C.; Dai, Z. R.; Charnvanichborikarn, S.; Carroll, S.
 307 A., Chemical and Mechanical Properties of Wellbore Cement Altered by CO₂-Rich Brine Using a
 308 Multianalytical Approach. *Environmental Science & Technology* **2013**, *47*, (3), 1745-1752.
- 309 3. Walsh, S. D. C.; Mason, H. E.; Du Frane, W. L.; Carroll, S. A., Experimental calibration of a
 310 numerical model describing the alteration of cement/caprock interfaces by carbonated brine. *Journal of*
 311 *Greenhouse Gas Control* **in review**.
- 312 4. Walsh, S. D. C.; Mason, H. E.; Du Frane, W. L.; Carroll, S. A., Mechanical and hydraulic
 313 coupling in cement-caprock interfaces exposed to carbonated brine. *Journal of Greenhouse Gas Control*
 314 **in review**.
- 315 5. Wigand, M.; Kaszuba, J. P.; Carey, J. W.; Hollis, W. K., Geochemical effects of CO₂
 316 sequestration on fractured wellbore cement at the cement/caprock interface. *Chemical Geology* **2009**, *265*,
 317 (1-2), 122-133.
- 318 6. Newell, D. L.; Carey, J. W., Experimental Evaluation of Wellbore Integrity Along the Cement-
 319 rock Boundary. *Environmental Science & Technology* **2013**, *47*, (1), 276-282.
- 320 7. Crow, W.; Williams, D. B.; Carey, J. W.; Celia, M.; Gasda, S., Wellbore integrity analysis of a
 321 natural CO(2) producer. In *Greenhouse Gas Control Technologies 9*, Gale, J.; Herzog, H.; Braitsch, J.,
 322 Eds. 2009; Vol. 1, pp 3561-3569.
- 323 8. Crow, W.; Carey, J. W.; Gasda, S.; Williams, D. B.; Celia, M., Wellbore integrity analysis of a
 324 natural CO₂ producer. *International Journal of Greenhouse Gas Control* **2010**, *4*, (2), 186-197.
- 325 9. Abdoulghafour, H.; Luquot, L.; Gouze, P., Characterization of the Mechanisms Controlling the
 326 Permeability Changes of Fractured Cements Flowed Through by CO₂-Rich Brine. *Environmental Science*
 327 *& Technology* **2013**, *47*, (18), 10332-10338.
- 328 10. Milestone, N. B.; Sugama, T.; Kukacka, L. E.; Carciello, N., CARBONATION OF
 329 GEOTHERMAL GROUTS .2. CO₂ ATTACK AT 150-DEGREES-C. *Cement and Concrete Research*
 330 **1986**, *16*, (6), 941-950.
- 331 11. Milestone, N. B.; Sugama, T.; Kukacka, L. E.; Carciello, N., CARBONATION OF
 332 GEOTHERMAL GROUTS .2. CO₂ ATTACK AT 250-DEGREES-C. *Cement and Concrete Research*
 333 **1987**, *17*, (1), 37-46.
- 334 12. Da Silva, J. R. M. C.; Milestone, N. B.; Johnston, J. H., The effect of drilling fluid and
 335 temperature on the cement-rock interaction in geothermal wells. In *Transactions - Geothermal Resources*
 336 *Council*, 2012; Vol. 36 1, pp 277-285.
- 337 13. Milestone, N. B.; Bigley, C. H.; Durant, A. T.; Sharp, M. D. W., Effects of CO₂ on geothermal
 338 cements. In *Transactions - Geothermal Resources Council*, 2012; Vol. 36 1, pp 301-306.
- 339 14. Pruess, K., Enhanced geothermal systems (EGS) using CO(2) as working fluid - A novel approach
 340 for generating renewable energy with simultaneous sequestration of carbon. *Geothermics* **2006**, *35*, (4),
 341 351-367.
- 342 15. Randolph, J. B.; Saar, M. O., Combining geothermal energy capture with geologic carbon dioxide
 343 sequestration. *Geophysical Research Letters* **2011**, *38*.
- 344 16. Carey, J. W.; Wigand, M.; Chipera, S. J.; WoldeGabriel, G.; Pawar, R.; Lichtner, P. C.; Wehner,
 345 S. C.; Raines, M. A.; Guthrie, G. D., Jr., Analysis and performance of oil well cement with 30 years Of
 346 CO₂ exposure from the SACROC Unit, West Texas, USA. *International Journal of Greenhouse Gas*
 347 *Control* **2007**, *1*, (1), 75-85.
- 348 17. Kutchko, B. G.; Strazisar, B. R.; Huerta, N.; Lowry, G. V.; Dzombak, D. A.; Thaulow, N., CO₂
 349 Reaction with Hydrated Class H Well Cement under Geologic Sequestration Conditions: Effects of
 350 Flyash Admixtures. *Environmental Science & Technology* **2009**, *43*, (10), 3947-3952.

18. Jung, H. B.; Jansik, D.; Um, W., Imaging Wellbore Cement Degradation by Carbon Dioxide under Geologic Sequestration Conditions Using X-ray Computed Microtomography. *Environmental Science & Technology* **2013**, *47*, (1), 283-289.
19. Jung, H. B.; Um, W., Experimental study of potential wellbore cement carbonation by various phases of carbon dioxide during geologic carbon sequestration. *Applied Geochemistry* **2013**, *35*, 161-172.
20. Long, H.; Swennen, R.; Foubert, A.; Dierick, M.; Jacobs, P., 3D quantification of mineral components and porosity distribution in Westphalian C sandstone by microfocus X-ray computed tomography. *Sedimentary Geology* **2009**, *220*, (1), 116-125.
21. Remeysen, K.; Swennen, R., Application of microfocus computed tomography in carbonate reservoir characterization: Possibilities and limitations. *Marine and Petroleum Geology* **2008**, *25*, (6), 486-499.
22. Wildenschild, D.; Sheppard, A. P., X-ray imaging and analysis techniques for quantifying pore-scale structure and processes in subsurface porous medium systems. *Advances in Water Resources* **2012**.
23. Cnudde, V.; Boone, M., High-resolution X-ray computed tomography in geosciences: a review of the current technology and applications. *Earth-Science Reviews* **2013**.
24. Ketcham, R. A.; Carlson, W. D., Acquisition, optimization and interpretation of X-ray computed tomographic imagery: applications to the geosciences. *Computers & Geosciences* **2001**, *27*, (4), 381-400.
25. Wellington, S.; Vinegar, H., X-ray computerized tomography. *Journal of Petroleum Technology* **1987**, *39*, (8), 885-898.
26. Walsh, S. D. C.; Du Frane, W. L.; Mason, H. E.; Carroll, S. A., Permeability of Wellbore-Cement Fractures Following Degradation by Carbonated Brine. *Rock Mechanics and Rock Engineering* **2013**, *46*, (3), 455-464.
27. Schindelin, J.; Arganda-Carreras, I.; Frise, E.; Kaynig, V.; Longair, M.; Pietzsch, T.; Preibisch, S.; Rueden, C.; Saalfeld, S.; Schmid, B.; Tinevez, J. Y.; White, D. J.; Hartenstein, V.; Eliceiri, K.; Tomancak, P.; Cardona, A., Fiji: an open-source platform for biological-image analysis. *Nature Methods* **2012**, *9*, (7), 676-682.
28. Henke, B. L.; Gullikson, E. M.; Davis, J. C., X-Ray Interactions: Photoabsorption, Scattering, Transmission, and Reflection at $E = 50\text{-}30,000$ eV, $Z = 1\text{-}92$. *Atomic Data and Nuclear Data Tables* **1993**, *54*, (2), 181-342.
29. Hubbell, J. H.; Seltzer, S. M. *Tables of X-ray mass attenuation coefficients and mass energy-absorption coefficients 1 keV to 20 MeV for elements Z= 1 to 92 and 48 additional substances of dosimetric interest*; National Inst. of Standards and Technology-PL, Gaithersburg, MD (United States). Ionizing Radiation Div.: 1995.
30. Gallucci, E.; Scrivener, K., Crystallisation of calcium hydroxide in early age model and ordinary cementitious systems. *Cement and Concrete Research* **2007**, *37*, (4), 492-501.
31. Kjellsen, K. O.; Justnes, H., Revisiting the microstructure of hydrated tricalcium silicate—a comparison to Portland cement. *Cement and Concrete Composites* **2004**, *26*, (8), 947-956.
32. Diamond, S., Calcium hydroxide in cement paste and concrete- a microstructural appraisal. *Materials Science of Concrete Special* **2001**, 37-58.

Determination of diffusion profiles in altered wellbore cement using XRCT methods

Harris E. Mason^{1,}, Stuart D. C. Walsh¹, Wyatt L. DuFrane¹, and Susan A. Carroll¹*

¹Physical and Life Sciences Directorate, Lawrence Livermore National Laboratory

*corresponding author: mason42@llnl.gov

Supporting Information

Figures

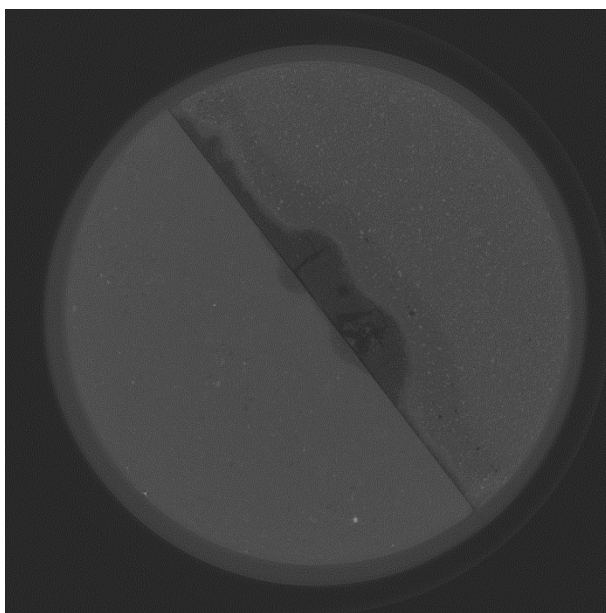


Figure S1: Example of a preprocessed image slice showing both the caprock (bottom left) and cement halves (top right). The lighter gray ring surrounding the sample is a Viton jacket used to contain pressure and fluid flow during the core flood experiment.

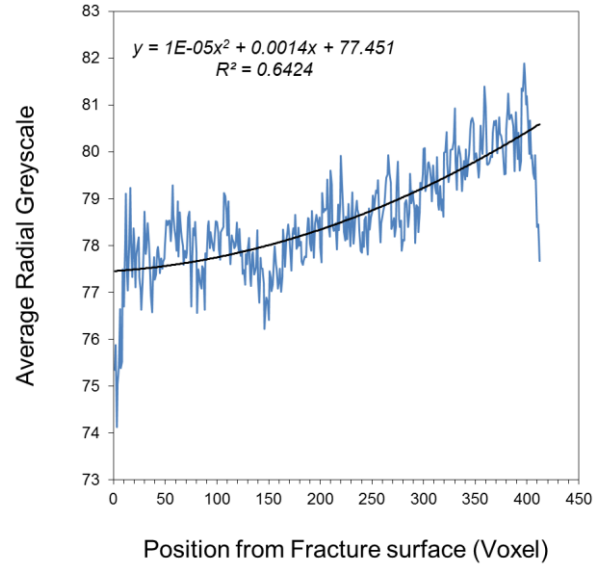
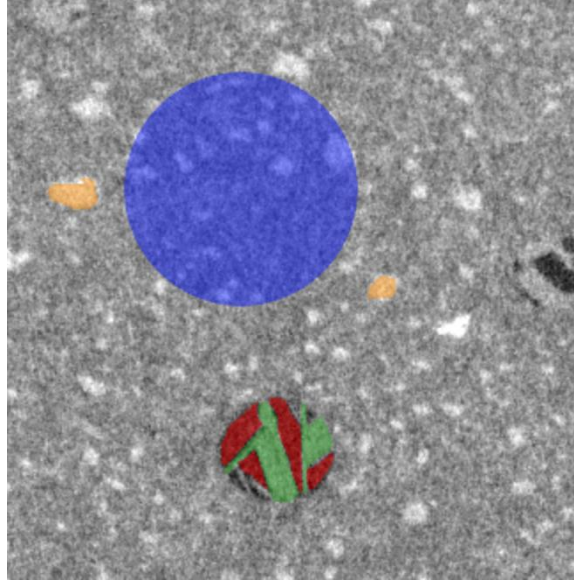


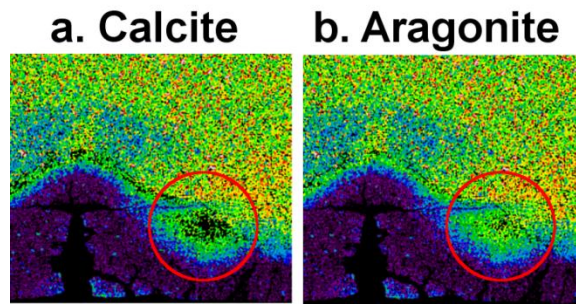
Figure S2: Grayscale profile averaged radially over the caprock region of an image slice (blue line). The solid line represents a least squares fit to the data and was used to correct the images for the effects of beam hardening.



411

412 **Figure S3.** Examples of areas used for the ELAC/Grayscale calibration. Grayscales were
 413 derived by averaging over the areas illustrated by the colored overlays. Orange: C_3S , Blue:
 414 Unreacted Cement, Green: CSH, Red: pore space. Additional areas were chosen corresponding
 415 to the average of the amorphous material, and pyrite grains in the caprock half.

416



417

418

Figure S4. False color images comparing the calculated grayscale for the reacted cement

419

assuming the calcium carbonate layer consists of **a.** calcite or **b.** aragonite. Red circle points out

420

an area of interest where the two images mismatch.

421